Measuring the internal temperature of a levitated nanoparticle in high vacuum

Erik Hebestreit, René Reimann, Martin Frimmer, and Lukas Novotny
Photonics Laboratory, ETH Zürich, 8093 Zürich, Switzerland

(Received 26 December 2017; published 5 April 2018)

The interaction of an object with its surrounding bath can lead to a coupling between the object's internal degrees of freedom and its center-of-mass motion. This coupling is especially important for nanomechanical oscillators, which are among the most promising systems for preparing macroscopic objects in quantum mechanical states. Here we exploit this coupling to derive the *internal* temperature of a levitated nanoparticle from measurements of its center-of-mass dynamics. For a laser-trapped silica particle in high vacuum, we find an internal temperature of 1000(60) K. The measurement and control of the internal temperature of nanomechanical oscillators is of fundamental importance because black-body emission sets limits to the coherence of macroscopic quantum states.

DOI: 10.1103/PhysRevA.97.043803

I. INTRODUCTION

Nanomechanical oscillators are used for inertial sensing and for the ultrasensitive measurement of forces and masses [1–6]. Especially impressive are the latest advances to use them for producing and sensing mechanical quantum states [7]. Among these oscillators, nanoparticles that are levitated in a strongly focused laser beam in vacuum stand out by lacking a mechanical clamping mechanism [8,9], which makes them promising candidates for quantum interference experiments with macroscopic objects [10–12]. Recently, the center-of-mass (COM) temperature T_{com} of these levitated optomechanical systems has been reduced to only a few phonons using parametric [8,9,13], or cavity-based cooling schemes [14–16], and is therefore quickly approaching the quantum regime.

Quantum states of such mesoscopic mechanical objects are extremely sensitive to decoherence, arising from any interaction of the object with its environment. For example, at finite pressure, random collisions with residual gas molecules decohere the mechanical motion. In ultrahigh vacuum, the radiation-pressure shot noise of the trapping laser is the dominant fluctuating force [13]. Importantly, even in the absence of a trapping laser, for example, during a matter-wave-interference free-fall experiment [11,17,18], there is a decoherence mechanism at work. This mechanism is the recoil force stemming from emitted black-body photons due to the finite internal temperature of the trapped particle. In high vacuum, where thermal emission is the only cooling channel for the internal particle temperature, even a minute absorption of the trapping laser by the particle can lead to an elevated internal temperature of a levitated object [10,11,18–23]. With the internal temperature limiting the lifetime of mesoscopic mechanical quantum states, the measurement and control of this internal temperature is a crucial prerequisite for future quantum interference experiments.

Moreover, even for levitated sensors in the classical regime, the internal temperature plays a central role. For instance, high internal temperatures are suspected to be the cause of particle loss at reduced gas pressures in numerous implementations [19–21]. Furthermore, a coupling between the internal temperature and the COM motion has become apparent in earlier studies of levitated particles at pressures above 1 mbar [19]. This coupling leads to increased COM temperatures, which implies a reduced force sensitivity of levitated sensors [20,24]. Despite its evident importance in the field of levitated optomechanics, the internal temperature and its influence on the COM motion has not yet been studied in the high-vacuum regime below 10^{-3} mbar, where the exceptional quality factors of levitated systems can be exploited for ultrasensitive measurements, cooling of the COM temperature, and the future creation of mechanical quantum states.

In this work, we measure the internal particle temperature in high vacuum (10^{-3} to 10^{-6} mbar) by selectively heating the particle with an infrared laser that is much lower in power than the trapping laser. Accordingly, this separate heating laser allows us to vary the internal particle temperature without affecting the trapping potential. By measuring the thermal relaxation dynamics of the particle's COM motion at varying internal temperatures, we quantify the influence of the particle's internal temperature on its COM dynamics. We model the interactions of an internally hot particle with a dilute gas [19] to determine the internal particle temperature and the energy accommodation coefficient, which characterizes the energy transfer between the particle's internal degrees of freedom and the surrounding gas.

II. EXPERIMENTAL SYSTEM

Figure 1 shows our experimental setup. We use a Nd:YAG laser operating at a wavelength of 1064 nm with a power of 70 mW that we focus with an objective (numerical aperture 0.8) to optically trap a SiO_2 nanoparticle with a nominal radius of $R = 68$ nm inside a vacuum chamber. All data shown in this work are recorded using the same nanoparticle. Besides small variations in mass from particle to particle, we find identical results when using different particles. In forward direction, the scattered light is collected with an aspheric lens to detect the particle position along three axes (x,y,z) with a balanced detection scheme [9]. For small oscillation amplitudes, the COM motion of the levitated nanoparticle along the coordinate

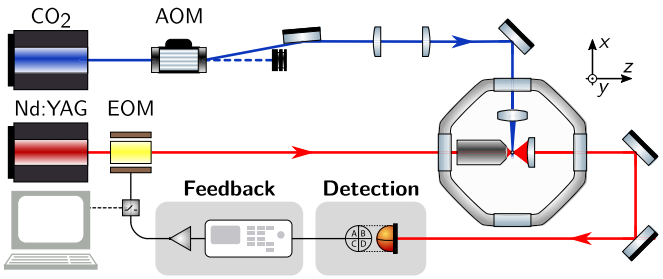

FIG. 1. Experimental setup. In the focus of a 1064-nm laser (red), we trap a SiO_2 nanoparticle. The trap is placed in a vacuum chamber to adjust the gas pressure. The light scattered by the particle is collected and detected with a balanced detector. A switchable parametric feedback allows us to cool the particle motion by modulating the laser beam intensity with an electro-optic modulator (EOM). To increase the internal temperature of the particle, we irradiate it from the side with a CO_2 laser (blue) whose intensity we adjust with an acousto-optic modulator (AOM).

x (equivalently for y and z) follows the equation of motion of a damped harmonic oscillator

$$m\ddot{x} + m\gamma\dot{x} + m\Omega_0^2 x = F_{\mathrm{fluct}}(t)\,. \tag{1}$$

Here, m is the particle mass, γ is the damping rate, and Ω_0 is the oscillation frequency. Typical mechanical oscillation frequencies $\Omega_0/2\pi$ are 125, 150, and 40 kHz for the oscillations in x, y, and z directions, respectively. The random fluctuating force $F_{\mathrm{fluct}}(t)$ describes the particle's interactions with the environment. Throughout this work, we operate in a pressure range of 10^{-3} to 10^{-6} mbar, where these interactions are dominated by collisions with gas molecules. In thermal equilibrium, the particle's COM motion is characterized by the temperature T_{com}, which equals the bath temperature of the gas T_{bath}. The COM temperature is given by $T_{\mathrm{com}} = m\langle\dot{x}^2\rangle/k_{\mathrm{B}}$, where $\langle\dot{x}^2\rangle$ is the variance of the particle velocity and k_{B} is the Boltzmann constant [25]. Using this relation between bath temperature and oscillation amplitude, we calibrate our detector signal at a pressure of 10 mbar, where the gas temperature can be considered in equilibrium with room temperature. Subsequently, we transfer this calibration to low pressure by measuring the particle's response to an electric field as detailed in Ref. [25]. Using the position information obtained from the light scattered by the particle, we apply a parametric feedback in order to cool the particle's COM temperature to $T_{\mathrm{com}} \ll T_{\mathrm{bath}}$ [9]. Table I gives an overview of relevant parameters used in this work.

To control the internal temperature T_{int} of the optically levitated nanoparticle without changing the optical trapping potential, we use a CO_2 laser with a wavelength of 10 μm (blue beam in Fig. 1) that illuminates the particle perpendicular to the propagation direction of the trapping beam. We adjust the CO_2 laser intensity $I_{\mathrm{CO_2}}$ using an acousto-optic modulator (AOM). At a wavelength of 10 μm, the optical absorption of silica is more than 7 orders of magnitude larger than at 1064 nm [26]. Therefore, a weakly focused CO_2 laser beam (numerical aperture 0.06) with a peak intensity $I_{\mathrm{CO_2}} < 1\,\mu\mathrm{W}/\mu\mathrm{m}^2$ is sufficient to tune the particle's internal temperature for our experiments. Importantly, the optical forces generated by the CO_2 laser on the particle are negligible. We estimate that the stiffening of the trapping potential due to the CO_2 laser causes a shift of the oscillation frequency of less than 0.1 mHz and the radiation pressure of the CO_2 laser results in a displacement of the equilibrium position of 20 fm.

III. MEASUREMENT OF PARTICLE DYNAMICS

Using the optical levitation setup described above, we investigate the coupling between the particle's internal temperature and its COM motion. To measure the COM dynamics of the particle, we perform relaxation experiments that are described in Sec. III A. In Sec. III B, we determine the change of the particle's internal temperature ΔT_{int} when activating the CO_2 laser from the change of the particle's oscillation frequency $\Delta\Omega_0$. Both measurements, performed at varying gas pressures and at different CO_2 laser intensities, allow us to deduce the absolute internal particle temperature T_{int} (see Sec. V).

A. Measurement of center-of-mass temperature

We investigate the coupling between the internal temperature and the COM motion of the particle by performing relaxation experiments. Each relaxation cycle starts with the

TABLE I. Important physical quantities used in this paper.

Symbol	Unit	Description
T_{com}	K	Temperature of the COM motion
T_{bath}	K	Effective bath temperature of gas in vacuum chamber
T_{int}	K	Internal temperature of the particle (in absence of CO_2 laser illumination)
Ω_0	Hz	Natural oscillation frequency
γ	Hz	COM gas damping rate (inverse of relaxation time)
Γ	Hz	COM single-phonon heating rate due to interactions with the gas
Γ'	K/s	Gas energy heating rate (at which the COM temperature increases)
$I_{\mathrm{CO_2}}$	W/m^2	Peak intensity of the CO_2 laser in the focus (at the particle position)
$\Delta\Omega_0$	Hz	Shift of natural oscillation frequency due to increasing T_{int} with the CO_2 laser
ΔT_{int}	K	Change of internal particle temperature due to CO_2 laser irradiation
α_{G}	1	Energy accommodation coefficient (energy transfer between gas and particle)
T_{im} (T_{em})	K	Temperature of the gas molecules impinging on (emerging from) the particle
γ_{im} (γ_{em})	Hz	COM damping rate caused by impinging (emerging) gas molecules
Γ'_{im} (Γ'_{em})	K/s	COM energy heating rate caused by impinging (emerging) gas molecules

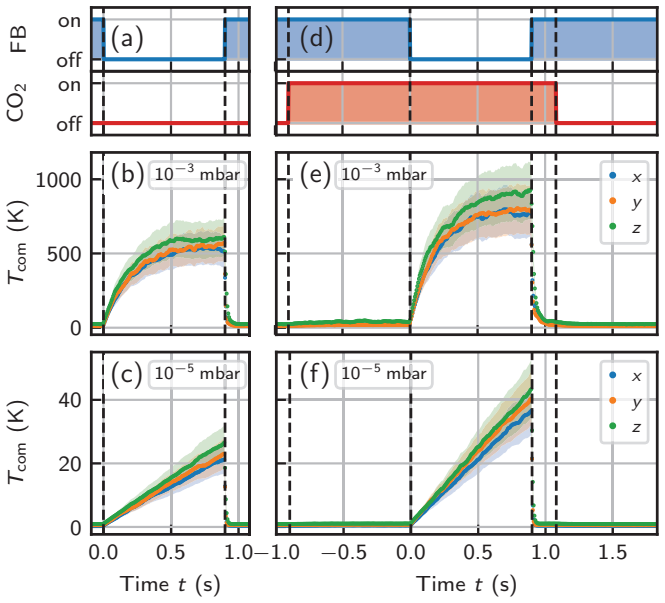

FIG. 2. Relaxation experiments. (a) Using parametric feedback (FB), we first cool the particle's COM motion. We switch the feedback off at time $t = 0$, such that the particle's average COM energy equilibrates toward the effective bath temperature. After 900 ms, the feedback is turned on again to return to the initial conditions. (b) At a pressure of 1×10^{-3} mbar, we observe a relaxation of the COM temperature T_{com} to the bath temperature T_{bath} along all three oscillation axes. (c) When reducing the pressure to 1×10^{-5} mbar, we only observe the initial slope of the relaxation curve that rises linearly with the heating rate Γ'. (d) For measuring the particle dynamics at elevated internal temperatures, we activate the CO_2 laser 900 ms before starting the relaxation experiment. (e) At 10^{-3} mbar, in the presence of the CO_2 heating laser, the particle's COM temperature equilibrates to a bath temperature higher than in the absence of the heating laser. (f) At 10^{-5} mbar, the slope of the heating curve Γ' is larger in the presence of the heating laser as compared to panel (c), where the heating laser is off. Quantities extracted from these measurements are summarized in Table II.

particle under parametric feedback cooling along all three oscillation axes. We switch off the feedback and let the particle's COM motion relax from a feedback-cooled state with $T_{com} \ll T_{bath}$ to the bath temperature T_{bath} of the surrounding gas. From the evolution of the COM temperature, we extract the damping rate γ and T_{bath}, which describe the particle's dynamics according to Eq. (1). These two quantities determine the single-phonon heating rate $\Gamma = \gamma k_B T_{bath}/(\hbar\Omega_0)$, which is the rate at which phonons enter the COM oscillation mode. Γ is a measure for the interaction strength of the particle's COM motion with its environment [27].

In Fig. 2(a), we show our experimental protocol for a single relaxation cycle in absence of CO_2 laser heating, consisting of three steps: (1) initializing the particle's COM temperature $T_{com}(t = 0)$ well below the bath temperature T_{bath} with the parametric feedback (FB), (2) switching off the feedback at time $t = 0$ to allow for a relaxation of the particle's COM temperature to the bath temperature, and (3) reactivating the feedback after 900 ms. During each relaxation cycle, we record a time trace of the particle's position, from which

TABLE II. Experimental and fitting parameters for the measurements in Fig. 2. The change in internal particle temperature ΔT_{int} is determined according to Sec. III B.

Fig.	p_{gas} (mbar)	I_{CO_2} $\left(\frac{\mu W}{\mu m^2}\right)$	ΔT_{int} (K)	T_{bath} (K)	$\gamma/(2\pi)$ (Hz)	$\Gamma'/(2\pi)$ $\left(\frac{K}{s}\right)$
2(b)	1×10^{-3}	0		571(21)	0.79(2)	451(29)
2(e)	1×10^{-3}	0.47	601(16)	824(34)	0.88(2)	723(43)
2(c)	1×10^{-5}	0				4.4(2)
2(f)	1×10^{-5}	0.47	825(17)			7.3(3)

we calculate its kinetic energy in sections of 6 ms [25]. In Fig. 2(b), we plot, for a pressure of $p_{gas} = 1\times10^{-3}$ mbar, the COM temperature that we obtain as an average over the kinetic energy of 1000 realizations of the relaxation cycle. We observe that after turning the parametric feedback off at $t = 0$, the COM temperature in all three axes rises at the same rate and asymptotically approaches a steady-state temperature of $T_{bath} = 571(21)$ K. Importantly, this bath temperature is significantly higher than the surrounding temperature of 300 K. Thus, the bath temperature felt by the particle is not the surrounding temperature, but an *effective* bath temperature. We reason in Sec. IV that the increased bath temperature is caused by an elevated internal temperature of the particle. When switching the feedback on again, the COM temperature is cooled to $T_{com} < 10$ K, such that the system is initialized for the next experimental cycle.

The temporal evolution of the COM temperature is described by the rate equation [13,27]

$$\frac{d}{dt}T_{com}(t) = -\gamma T_{com}(t) + \Gamma'. \tag{2}$$

Here, for convenience, instead of using the single-phonon heating rate Γ in units of Hertz, we define an energy heating rate $\Gamma' = \Gamma\hbar\Omega_0/k_B = \gamma T_{bath}$ in units of K/s. The first term on the right-hand side of Eq. (2) describes the dissipation of energy from the COM oscillation, while the second term characterizes the rate at which energy enters the oscillation mode from the environment. For $dT_{com}/dt = 0$, we find that the COM temperature equals the bath temperature $T_{bath} = \Gamma'/\gamma$. Solving Eq. (2) yields the evolution from the initial COM temperature $T_{com}(t = 0)$ as

$$T_{com}(t) = T_{bath} + [T_{com}(0) - T_{bath}]e^{-\gamma t}. \tag{3}$$

We fit Eq. (3) to the measured relaxation curves shown in Fig. 2(b) to extract the damping rate $\gamma/2\pi = 0.79(2)$ Hz, and derive a heating rate of $\Gamma'/(2\pi) = T_{bath}\gamma/(2\pi) = 451(29)$ K/s. We summarize all the measurement results from Fig. 2 in Table II.

When lowering the gas pressure to 1×10^{-5} mbar, as shown in Fig. 2(c), we observe relaxation dynamics that are 100 times slower than those at 1×10^{-3} mbar such that letting the particle reheat close to its steady-state COM temperature would require 100 s for a single relaxation cycle and sufficiently many experimental cycles to average out the thermal fluctuations would take prohibitively long. Therefore, at low pressures,

where $\gamma^{-1} \gg 1\,\mathrm{s}$, we only capture the linear beginning of the relaxation curve, where the COM temperature evolves as $T_{\mathrm{com}}(t) \approx T_{\mathrm{com}}(0) + \Gamma' t$. We find that the slope of the COM temperature in Fig. 2(c) corresponds to a heating rate of $\Gamma'/(2\pi) = 4.4(2)\,\mathrm{K/s}$. Comparing the heating rates obtained from the experiments shown in Figs. 2(b) and 2(c) shows that Γ' scales linearly with pressure. Given the linear pressure dependence of the damping rate γ, this suggests a pressure-independent bath temperature T_{bath}, which can be attributed to the absence of convective cooling at pressures below 10^{-3} mbar (see Sec. VI) [9,13].

Up to this point, we considered the particle in the absence of additional heating by CO_2 laser irradiation. In order to study the influence of the internal particle temperature T_{int} on the dynamics, we repeat the relaxation experiments with an elevated internal particle temperature. Each relaxation cycle follows the sequence shown in Fig. 2(d): We start with the particle in a feedback-cooled state and activate the CO_2 laser at $t = -0.9\,\mathrm{s}$. Experimentally, we find that the particle's internal temperature equilibrates within a few 100 ms (cf. Sec. III B) [18]. We therefore wait for 900 ms, before switching off the feedback at time $t = 0$ for 900 ms. After the relaxation cycle, we switch off the CO_2 laser at time $t = 1.08\,\mathrm{s}$ to let the particle's internal temperature cool down to its initial value. In Fig. 2(e), we show the temperature relaxation along the three axes of the COM motion at a pressure of 1×10^{-3} mbar for a particle heated with the CO_2 laser. We observe a relaxation to a COM temperature of $T_{\mathrm{bath}} = 824(34)\,\mathrm{K}$, which is higher than that observed in the absence of additional heating [cf. Fig. 2(b)]. This shows that increasing the internal particle temperature effectively causes a rise in the extracted bath temperature T_{bath}. Furthermore, we measure a higher damping rate γ in the case with additional heating, which results in an increase of the heating rate Γ' by 60(14)% compared to Fig. 2(b) in the absence of CO_2 laser heating (see Table II). Accordingly, an increased internal temperature T_{int} of the trapped particle gives rise to an increased (effective) bath temperature T_{bath}, entailing an increased heating rate Γ'.

In Fig. 2(f), we plot the measured relaxation curves for the internally heated particle at 1×10^{-5} mbar. We observe, in agreement with the results at 1×10^{-3} mbar, that the heating rate Γ' increases by 66(10)% in comparison with the results in Fig. 2(c) for the nonheated particle (see Table II).

To determine the particle's COM dynamics at different pressures and internal temperatures, we perform relaxation measurements in a pressure range between 5×10^{-7} and 3×10^{-3} mbar. Furthermore, we vary the intensity in the focus of the CO_2 laser from 0 to $0.47\,\mu\mathrm{W}/\mu\mathrm{m}^2$. To account for possible drifts of the experimental setup, we recalibrated our detectors at 1×10^{-3} and 1×10^{-5} mbar. In Fig. 3(a), we summarize the measured heating rates for different pressures. Below 10^{-3} mbar, the heating rate depends linearly on the gas pressure. Furthermore, the heating rates under illumination with the CO_2 laser (orange) are consistently higher than for the case without increasing the internal temperature (blue). The dependence of the heating rate on the peak intensity of the CO_2 laser is shown in Fig. 3(b). Our measurements show a clear dependence of the COM dynamics on CO_2 laser irradiation, which suggests a coupling between the COM motion and the particle's internal temperature.

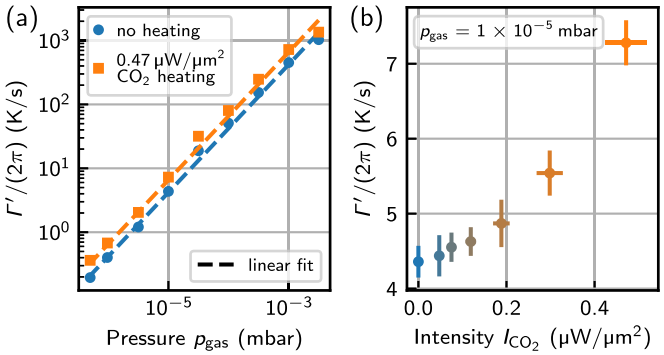

FIG. 3. (a) Heating rates as a function of pressure extracted from relaxation measurements without additional heating of the internal temperature (blue) and with maximal heating (CO_2 laser intensity of $I_{\mathrm{CO_2}} = 0.47\,\mu\mathrm{W}/\mu\mathrm{m}^2$, orange). The dashed lines are linear fits to the data points. Error bars are smaller than the marker size. (b) Heating rates at different intensities of the CO_2 laser measured at a pressure of 1×10^{-5} mbar. The error bars indicate the standard deviation of the measurements.

B. Measurement of internal temperature change

Increasing the internal particle temperature in a controlled way with the CO_2 laser enables us to study the dependence of the particle dynamics on the internal particle temperature T_{int}. For a quantitative analysis, we additionally require an independent measurement of the increase of the internal particle temperature ΔT_{int} due to the CO_2 laser irradiation. We deduce the change in the internal temperature using the temperature dependence of the particle's material properties. In particular, we exploit the temperature dependence of the mass density ρ [28] and the refractive index n [29] of silica. These material properties lead to a temperature-dependent oscillation frequency Ω_0 of the particle, which scales as $\Omega_0 \propto \sqrt{\rho^{-1}(n^2-1)/(n^2+2)}$ [9]. In Fig. 4(a), we plot as a blue line the calculated relative shift of the particle's oscillation frequency $\Delta\Omega_0/\Omega_0$ as a function of the internal particle temperature T_{int} according to the material data listed in Refs. [28,29], where Ω_0 denotes the oscillation frequency at an internal temperature of 300 K. The relative oscillation-frequency shift depends almost linearly on the internal particle temperature T_{int} and we find a proportionality factor $\Delta\Omega_0/\Omega_0 = 1.43(1)\times10^{-5}\,\mathrm{K}^{-1}\times\Delta T_{\mathrm{int}}$. Accordingly, we can determine the relative increase in internal temperature of the particle ΔT_{int} caused by the irradiation by the CO_2 laser from the relative shift of the particle oscillation frequency. This assumes that the internal temperature is homogeneous across the particle [19]. Furthermore, since there are no data available for the refractive index n of glass above 1000 K, we extend the linear trend of the relative frequency change found in Fig. 4(a) to a temperature of 1800 K, the highest internal particle temperature occurring in this work.

In Fig. 4(b), we show the measured relative change in oscillation frequency as a function of time when heating the particle with different CO_2 laser intensities at a pressure of 1×10^{-3} mbar. We perform repeated heating cycles, where we start with the particle's COM motion being feedback cooled and the heating laser being switched off. We activate the CO_2 laser from $t = -0.9\,\mathrm{s}$ to 1.08 s [cf. Figs. 2(d) and 2(e)], in

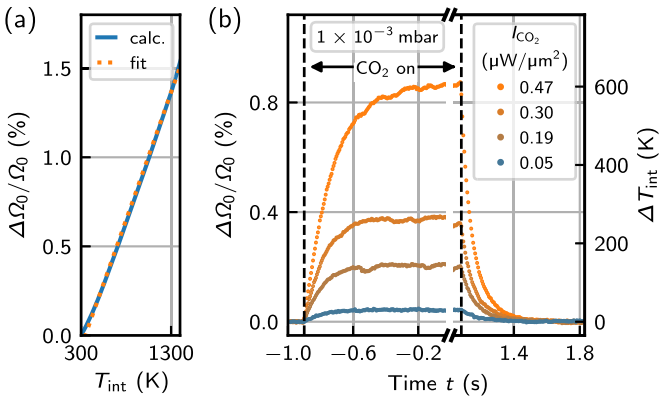

FIG. 4. (a) Calculated temperature dependence of oscillation frequency. When the particle is heated with the CO_2 laser, its oscillation frequency increases due to changes in the particle's material properties. This leads to a nearly linear relation between relative frequency change and increase of the internal particle temperature with $\Delta\Omega_0/\Omega_0 = (1.43\times10^{-5}\,\mathrm{K}^{-1})\Delta T_{\mathrm{int}}$, where Ω_0 denotes the oscillation frequency at an internal particle temperature of 300 K. (b) Measured relative frequency shift due to heating of particle with CO_2 laser for different heating laser powers at a pressure of 1×10^{-3} mbar. Here, Ω_0 is the particle oscillation frequency without CO_2 laser irradiation. The time axis corresponds to the one shown in the relaxation cycle in Fig. 2(e). According to the functional dependence extracted from panel (a), the maximally observed frequency shift corresponds to a temperature rise of $\Delta T_{\mathrm{int}} = 601(16)$ K.

order to illuminate the particle with a CO_2 laser intensity of up to $I_{CO_2} = 0.47\,\mu\mathrm{W}/\mu\mathrm{m}^2$. During the entire heating cycle, we record the COM position of the particle along the three axes, extract the oscillation frequency from segments of 6 ms length, and average each segment over 1000 realizations. We calculate the relative change of the oscillation frequency and average over the three oscillation axes. After activating the CO_2 laser, we find an upshift of the oscillation frequency of up to 0.9% for the maximum CO_2 laser intensity. We interpret this frequency shift as an increase of the internal particle temperature due to absorption heating. Applying the linear conversion factor of $1.43\times10^{-5}\,\mathrm{K}^{-1}$ found in Fig. 4(a), we obtain a change in the particle's internal temperature of $\Delta T_{\mathrm{int}} = 601(16)$K. Using higher CO_2 laser intensities causes particle loss during the heating cycle. We attribute these losses to strong changes in material properties when reaching the working point of glass, or to the high COM oscillation amplitudes due to the elevated internal temperature of the particle.

IV. TWO-BATH MODEL OF GAS INTERACTIONS

Having established experimental methods to measure the particle's COM dynamics and the change of its internal temperature ΔT_{int} due to CO_2 laser irradiation, in the following, we develop a theoretical model to extract the internal particle temperature T_{int} at any gas pressure. We describe the interaction of an internally hot particle with the surrounding gas following the model developed in Ref. [19]. It assumes an *inelastic* scattering process, that is, an impinging gas molecule with temperature T_{im} heats up to a temperature T_{em} upon interacting with the hot particle. As a consequence, the particle interacts with two different baths, the bath of impinging molecules with parameters T_{im}, γ_{im}, and Γ'_{im} and the bath of emerging gas molecules with parameters T_{em}, γ_{em}, and Γ'_{em} [30]. Therefore, the total gas damping rate is $\gamma = \gamma_{\mathrm{im}} + \gamma_{\mathrm{em}}$ and the total gas heating rate equals $\Gamma' = \Gamma'_{\mathrm{im}} + \Gamma'_{\mathrm{em}} = T_{\mathrm{im}}\gamma_{\mathrm{im}} + T_{\mathrm{em}}\gamma_{\mathrm{em}}$ [19]. The damping rate associated with the emerging gas molecules is $\gamma_{\mathrm{em}} = \pi\sqrt{T_{\mathrm{em}}/T_{\mathrm{im}}}\gamma_{\mathrm{im}}/8$ and the damping rate due to the impinging gas molecules is $\gamma_{\mathrm{im}} = 32R^2 p_{\mathrm{gas}}/(3m\bar{v}_{\mathrm{gas}})$. Here, $\bar{v}_{\mathrm{gas}} = \sqrt{8N_{\mathrm{A}}k_{\mathrm{B}}T_{\mathrm{im}}/(\pi M)}$ is the mean velocity of gas molecules, where M is the molar mass of the gas and N_{A} is Avogadro's constant [19]. Introducing the energy accommodation coefficient $\alpha_G = (T_{\mathrm{em}} - T_{\mathrm{im}})/(T_{\mathrm{int}} - T_{\mathrm{im}})$, which describes the energy transfer from the particle to the gas, we find that the total heating rate follows

$$\Gamma' = \gamma_{\mathrm{im}}\left\{T_{\mathrm{im}} + \frac{\pi}{8}\frac{[\alpha_G T_{\mathrm{int}} + (1-\alpha_G)T_{\mathrm{im}}]^{3/2}}{\sqrt{T_{\mathrm{im}}}}\right\}. \quad (4)$$

It depends on the particle's properties (radius, mass, and internal temperature), the gas properties (pressure, temperature, and composition), and the energy transfer between particle and gas. This two-bath model predicts that increasing the particle's internal temperature T_{int} causes a rise of the gas heating rate Γ', which is what we observe experimentally in Fig. 2. In particular, as described in the following section, we are able to derive the internal temperature of the particle using the measured heating rates [cf. Fig. 3(a)].

V. INTERNAL PARTICLE TEMPERATURE

According to Eq. (4), the heating rate depends on the internal temperature of the particle T_{int}, the energy accommodation coefficient α_{G}, the molar mass of the gas M, and the temperature of the impinging gas molecules T_{im}, which equals the temperature of the vacuum chamber walls and is measured throughout the experiment. To determine the molar mass M of the gas, we measure the gas composition at pressures below 10^{-3} mbar with a residual gas analyzer. We find that the gas consists to 58(9)% of water vapor and contains in addition nitrogen, hydrogen, oxygen, and carbon dioxide. We deduce an average molar mass of $M = 20(11)$ g/mol. The energy accommodation coefficient α_G also depends on the gas composition in the vacuum chamber. However, as the energy accommodation coefficient of water vapor on silica is not known, for now, we assume a value of $\alpha_G = 0.65$. At the end of this section, we justify this choice by determining the accommodation coefficient α_G from the experimental data.

We deduce the internal particle temperature T_{int} from the measured heating rates in two ways: (i) from the absolute measured heating rates Γ' in the absence of CO_2 laser heating and (ii) using the heating rate measured at varying internal temperatures $T_{\mathrm{int}} + \Delta T_{\mathrm{int}}$, where the change in the internal temperature is known from the oscillation frequency shift (see Sec. III B). For method (i), we solve Eq. (4) for T_{int} and use the heating rates measured in Fig. 3(a) (blue data points). In Fig. 5(a), we plot in blue the internal temperature that we extract with this method for different gas pressures. We obtain temperature values that are distributed between 600 and 1400 K.

For method (ii), we compute the ratio of the measured heating rate $\Gamma'^{\mathrm{CO_2}}$ in the presence of the CO_2 heating laser

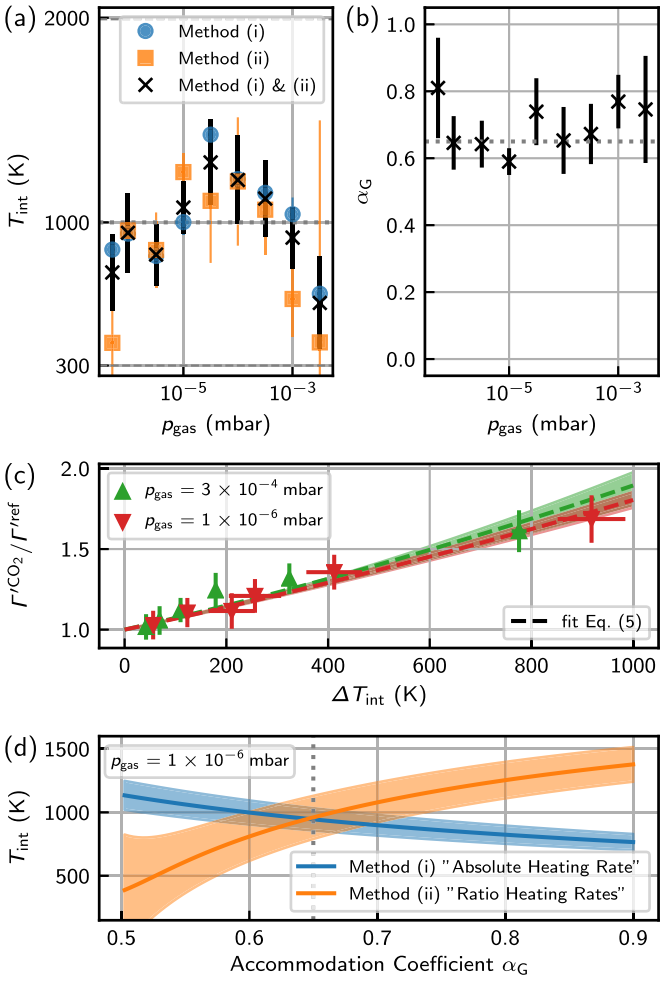

FIG. 5. (a) Internal particle temperatures derived using different methods: (i) using the absolute heating rate of the internally nonheated particle (blue), (ii) using the ratio of heating rates for an internally heated and internally nonheated particle (orange). The combination of methods (i) and (ii) is shown in black [see panel (d)]. Marked are room temperature (300 K), the melting temperature of silica (∼2000 K), and the average of the internal temperatures $T_{int} = 1000(60)$ K at pressures below 10^{-3} mbar. (b) Corresponding to the combined method in panel (a), we plot the deduced energy accommodation coefficients and mark their mean value $\alpha_G = 0.65(3)$. (c) To illustrate method (ii), we plot the ratio of the heating rates with and without the CO_2 laser illuminating the particle as a function of ΔT_{int} for two pressures. To each dataset, we fit Eq. (5) and infer an internal particle temperature T_{int} as a fit parameter. (d) Combining methods (i) and (ii), we plot the derived internal particle temperature depending on the chosen accommodation coefficient for methods (i) and (ii) at a pressure of 1×10^{-6} mbar. From the intersection point, we infer the best-fit energy accommodation coefficient and the internal particle temperature [see panels (a) and (b), black data points]. The error bars and shaded areas in all plots indicate the 1σ confidence intervals.

and the heating rate Γ'^{ref} in the absence of the heating laser. From Eq. (4), we find the theoretical expression

$$\frac{\Gamma'^{CO_2}}{\Gamma'^{ref}} = \frac{\frac{8}{\pi}T_{im}^{3/2} + \left(T_{em}^{CO_2}\right)^{3/2}}{\frac{8}{\pi}T_{im}^{3/2} + \left(T_{em}^{ref}\right)^{3/2}}. \quad (5)$$

The temperature of the emerging gas molecules in the case with the activated CO_2 laser is $T_{em}^{CO_2} = \alpha_G(T_{int} + \Delta T_{int}) + (1-\alpha_G)T_{im}$ and without additional heating $T_{em}^{ref} = \alpha_G T_{int} + (1-\alpha_G)T_{im}$. We measure the change of internal temperature ΔT_{int} using the shift in oscillation frequency as described in Sec. III B. Accordingly, we can deduce the absolute internal particle temperature T_{int} as the only free parameter in Eq. (5). We plot the ratio of the heating rates with and without the CO_2 laser in Fig. 5(c) at 3×10^{-4} mbar (green) and at 1×10^{-6} mbar (red) for six different CO_2 laser intensities. To these data points we fit Eq. (5) (dashed lines). The shaded areas indicate the 1σ confidence interval of the fit. The only free parameter for the fits is the absolute internal temperature of the particle T_{int} in the absence of CO_2 laser irradiation. We plot these internal particle temperatures that were extracted with method (ii) in Fig. 5(a) in orange and find values in a similar range like for method (i).

So far, we have discussed two independent methods to determine the internal temperature of the particle using the absolute value of the heating rate or the ratio of the heating rates at different internal temperatures. However, in both cases we had to assume a value for the *a priori* unknown energy accommodation factor α_G. We now combine both methods to deduce both the internal particle temperature and the energy accommodation coefficient from the experimental data. In Fig. 5(d), we show for a pressure of 1×10^{-6} mbar the calculated internal particle temperature determined using the two methods for varying accommodation coefficients between $\alpha_G = 0.5$ and 0.9. While methods (i) and (ii) are independent, they should both yield the same result for the internal particle temperature. Accordingly, the intersection of both graphs in Fig. 5(d) provides the accommodation coefficient, where the results of both methods coincide. In this example at 1×10^{-6} mbar, we find $T_{int} = 950(200)$ K without the CO_2 laser activated, and $\alpha_G = 0.65(8)$. In Fig. 5(a), we plot in black the internal particle temperature that we determine using the combined method at the different gas pressures. We compare these measurements with the corresponding model in Sec. VI. In addition, in Fig. 5(b), we show the corresponding energy accommodation coefficient for the different gas pressures. For the energy accommodation coefficient, we do not find a significant trend when lowering the gas pressure, suggesting that in our setup below 10^{-3} mbar the relative gas composition does not depend on pressure. This conclusion is supported by our measurement of the gas composition using a residual gas analyzer. Accordingly, we deduce a mean energy accommodation factor of $\alpha_G = 0.65(3)$ by averaging over all the measurements in Fig. 5(b).

VI. THERMODYNAMIC ESTIMATIONS

Now that we are able to measure the internal particle temperature, we compare our results with theoretical thermodynamic estimations. We consider the following thermal absorption and emission processes that the particle experiences: The particle's internal energy increases due the to absorption of laser light and incident black-body radiation from the environment. On the other hand, the particle dissipates internal energy through black-body radiation and gas convection [10]. In thermodynamic equilibrium, we derive a steady-state internal temperature of the particle T_{int}.

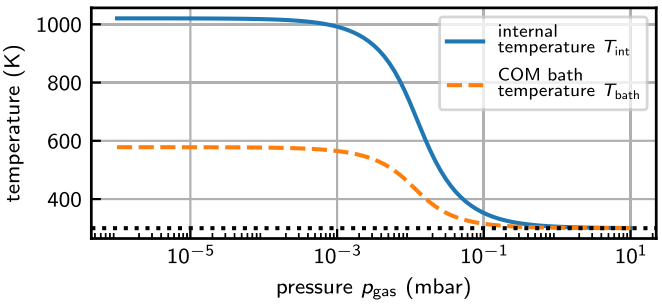

FIG. 6. Internal particle temperature calculated as a function of pressure from the balance of emission and absorption rates (blue solid line). At pressures above 10^{-1} mbar, convective gas cooling dominates the dissipation of internal energy and the internal particle temperature equilibrates to the environment temperature of 300 K (black dotted line). Below 10^{-3} mbar, convection is not efficient anymore and the internal temperature approaches 1020 K. Additionally, we calculate the resulting COM equilibrium temperature T_{bath} from the two-bath model (Sec. IV) using the parameters determined in the experiments (orange dashed line).

In Fig. 6, we plot the internal temperature for varying gas pressure that we calculate following Ref. [10] (blue solid line). Here, we assume an accommodation coefficient of $\alpha_G = 0.65$ as we measured before in Sec. V, and the refractive index of silica listed in Ref. [26]. This calculation shows that there is a transition from low internal temperatures at pressures above 1 mbar, where the dissipation of internal energy is dominated by gas convection, to high internal temperatures below 10^{-3} mbar, where the only efficient dissipation mechanism is black-body emission [20]. For our parameters, the equilibrium temperature at pressures below 10^{-3} mbar stabilizes at $T_{int} = 1020$ K. Therefore, we also expect a constant internal particle temperature for gas pressures below 10^{-3} mbar in our experiment. Computing the weighted average of the measured internal particle temperature below 10^{-3} mbar from Fig. 5(a) (black crosses), we find $T_{int} = 1000(60)$ K, which is in agreement with the thermodynamic estimate. We attribute the deviations of the data in Fig. 5(a) from this model to measurement uncertainty and drift of the calibration.

Additionally, we plot in Fig. 6 the expected effective COM bath temperature $T_{bath} = (T_{im}\gamma_{im} + T_{em}\gamma_{em})/(\gamma_{im} + \gamma_{em})$ (orange dashed line) for our experimental parameters and the energy accommodation factor of $\alpha_G = 0.65$ that we previously deduced from our measurements. The bath temperature approaches a value of 580 K at high vacuum, where convective cooling through the residual gas becomes negligible. This theoretical result is in agreement with our measurement in Fig. 2(b).

VII. CONCLUSION

We have shown that the coupling between the internal degrees of freedom of a levitated nanoparticle and its COM motion persists in a gas pressure range from 10^{-3} to 10^{-6} mbar. This coupling causes an elevated effective bath temperature above room temperature at high vacuum, which is of importance for levitated particle sensors as it decreases the sensitivity compared to an equivalent sensor at room temperature [20,24]. We expect this coupling to be present also for lower pressures, up to a point where interactions with the photon bath start to dominate the COM dynamics of the levitated particle [13]. In this lower pressure regime, other coupling mechanisms between the internal and COM temperature will become important, e.g., mediated through the recoil of black-body photons that depend on the internal particle temperature.

Furthermore, using the gas-mediated coupling and applying a model of the interaction of the particle with the surrounding dilute gas, we estimate the internal particle temperature. For our system, we deduce a mean internal particle temperature of $T_{int} = 1000(60)$ K at gas pressures below 10^{-3} mbar and an energy accommodation coefficient of $\alpha_G = 0.65(3)$. This high internal particle temperature is mainly caused by absorptive heating of the trapping laser and weak emission of black-body radiation. We point out that our method is not limited to determining the internal temperature of optically levitated silica nanoparticles, but is universally applicable to any other material system that can be levitated and COM cooled.

In view of future quantum interference experiments, which require internal particle temperatures well below room temperature to achieve superpositions larger than the particle diameter, our measurements underline the importance of developing methods to control the internal particle temperature, as decoherence due to black-body radiation prevents the appearance of interference patterns for high internal particle temperatures [11,12,31]. Cooling of the internal particle temperature, as demonstrated at high gas pressure for levitated systems with an internal level structure, could serve as a key technology to reduce those decoherence effects for optically levitated particles [23]. As the internal particle temperature is determined by the absorption of the trapping laser, one may consider combining different particle materials with suitable trapping wavelengths, such as silicon and telecom wavelength [18]. Further possibilities to reduce the internal particle temperature include alternative levitation strategies, such as Paul traps [16] and magnetic levitation [32].

ACKNOWLEDGMENTS

The authors acknowledge valuable discussions with C. Dellago, O. Romero-Isart, and J. Gieseler. We thank P. Kurpiers and A. Wallraff for lending us their residual gas analyzer. This work has been supported by ERC-QMES (No. 338763) and the Swiss National Centre of Competence in Research (NCCR) - Quantum Science and Technology (QSIT) program (No. 51NF40-160591).

[1] C. L. Degen, F. Reinhard, and P. Cappellaro, Rev. Mod. Phys. **89**, 035002 (2017).
[2] H. J. Mamin and D. Rugar, Appl. Phys. Lett. **79**, 3358 (2001).
[3] J. D. Teufel, J. W. Harlow, C. A. Regal, and K. W. Lehnert, Phys. Rev. Lett. **101**, 197203 (2008).
[4] K. Jensen, K. Kim, and A. Zettl, Nat. Nanotechnol. **3**, 533 (2008).

[5] G. Anetsberger, E. Gavartin, O. Arcizet, Q. P. Unterreithmeier, E. M. Weig, M. L. Gorodetsky, J. P. Kotthaus, and T. J. Kippenberg, Phys. Rev. A **82**, 061804 (2010).
[6] J. Moser, J. Güttinger, A. Eichler, M. J. Esplandiu, D. E. Liu, M. I. Dykman, and A. Bachtold, Nat. Nanotechnol. **8**, 493 (2013).
[7] J. Chan, T. P. M. Alegre, A. H. Safavi-Naeini, J. T. Hill, A. Krause, S. Gröblacher, M. Aspelmeyer, and O. Painter, Nature (London) **478**, 89 (2011).
[8] T. Li, S. Kheifets, and M. G. Raizen, Nat. Phys. **7**, 527 (2011).
[9] J. Gieseler, B. Deutsch, R. Quidant, and L. Novotny, Phys. Rev. Lett. **109**, 103603 (2012).
[10] D. E. Chang, C. A. Regal, S. B. Papp, D. J. Wilson, J. Ye, O. Painter, H. J. Kimble, and P. Zoller, Proc. Natl. Acad. Sci. USA **107**, 1005 (2010).
[11] O. Romero-Isart, A. C. Pflanzer, F. Blaser, R. Kaltenbaek, N. Kiesel, M. Aspelmeyer, and J. I. Cirac, Phys. Rev. Lett. **107**, 020405 (2011).
[12] M. Arndt and K. Hornberger, Nat. Phys. **10**, 271 (2014).
[13] V. Jain, J. Gieseler, C. Moritz, C. Dellago, R. Quidant, and L. Novotny, Phys. Rev. Lett. **116**, 243601 (2016).
[14] N. Kiesel, F. Blaser, U. Delic, D. Grass, R. Kaltenbaek, and M. Aspelmeyer, Proc. Natl. Acad. Sci. USA **110**, 14180 (2013).
[15] P. Asenbaum, S. Kuhn, S. Nimmrichter, U. Sezer, and M. Arndt, Nat. Commun. **4**, 2743 (2013).
[16] J. Millen, P. Z. G. Fonseca, T. Mavrogordatos, T. S. Monteiro, and P. F. Barker, Phys. Rev. Lett. **114**, 123602 (2015).
[17] L. Hackermüller, K. Hornberger, B. Brezger, A. Zeilinger, and M. Arndt, Nature (London) **427**, 711 (2004).
[18] J. Bateman, S. Nimmrichter, K. Hornberger, and H. Ulbricht, Nat. Commun. **5**, 4788 (2014).
[19] J. Millen, T. Deesuwan, P. Barker, and J. Anders, Nat. Nanotechnol. **9**, 425 (2014).
[20] G. Ranjit, D. P. Atherton, J. H. Stutz, M. Cunningham, and A. A. Geraci, Phys. Rev. A **91**, 051805 (2015).
[21] A. T. M. A. Rahman, A. C. Frangeskou, M. S. Kim, S. Bose, G. W. Morley, and P. F. Barker, Sci. Rep. **6**, 21633 (2016).
[22] M. L. Juan, G. Molina-Terriza, T. Volz, and O. Romero-Isart, Phys. Rev. A **94**, 023841 (2016).
[23] A. T. M. A. Rahman and P. F. Barker, Nat. Photon. **11**, 634 (2017).
[24] G. Ranjit, M. Cunningham, K. Casey, and A. A. Geraci, Phys. Rev. A **93**, 053801 (2016).
[25] E. Hebestreit, M. Frimmer, R. Reimann, C. Dellago, F. Ricci, and L. Novotny, arXiv:1711.09049 [Rev. Sci. Instrum. (to be published)].
[26] R. Kitamura, L. Pilon, and M. Jonasz, Appl. Opt. **46**, 8118 (2007).
[27] J. Gieseler, R. Quidant, C. Dellago, and L. Novotny, Nat. Nanotechnol. **9**, 358 (2014).
[28] R. Brückner, J. Non-Cryst. Solids **5**, 123 (1970).
[29] R. M. Waxler and G. Cleek, J. Res. Natl. Stand. Sec. A **77A**, 755 (1973).
[30] P. Epstein, Phys. Rev. **23**, 710 (1924).
[31] R. Kaltenbaek, G. Hechenblaikner, N. Kiesel, O. Romero-Isart, K. C. Schwab, U. Johann, and M. Aspelmeyer, Exp. Astron. **34**, 123 (2012).
[32] O. Romero-Isart, L. Clemente, C. Navau, A. Sanchez, and J. I. Cirac, Phys. Rev. Lett. **109**, 147205 (2012).